Rapid deformation of Kilauea Volcano: Global Positioning System measurements between 1990 and 1996

Susan Owen[1] and Paul Segall

Department of Geophysics, Stanford University, Stanford, California

Michael Lisowski, Asta Miklius, Roger Denlinger,[2] and Maurice Sako

U.S. Geological Survey, Hawaii National Park, Hawaii

Abstract. Campaign Global Positioning System (GPS) measurements from 1990 to 1996 are used to calculate surface displacement rates on Kilauea Volcano, Hawaii. The GPS data show that the south flank of the volcano, which has generated several large earthquakes in the past 3 decades, is displacing at up to ~8 cm/yr to the south-southeast. The summit and rift zones are subsiding, with maximum subsidence rates of ~8 cm/yr observed a few kilometers south of the summit caldera. Elastic dislocation modeling of the GPS data suggests that the active sources of deformation include deep rift opening along the upper east and east rift zone, fault slip along a subhorizontal fault near the base of the volcano, and deflation near the summit caldera. A nonlinear optimization algorithm was used to explore the parameter space and to find the best fitting source geometry. There is a broad range of model geometries that fit the data reasonably well. However, certain models can be ruled out, including those that have shallow rift opening or shallow fault slip. Some offshore, aseismic slip on a fault plane that dips between 25° north-northwest and 8° south-southeast is required. Best fitting slip and rift opening rates are 23–28 cm/yr, although rates as low as 10 cm/yr are permitted by the data.

1. Introduction

Kilauea Volcano is the youngest of five subaerial volcanoes on the island of Hawaii. As an actively erupting volcano, it attracts the attention of many scientists interested in magmatic processes. However, scientists were reminded of another process active within Kilauea on November 29, 1975, when a $M7.2$ earthquake shook Kilauea and the nearby city of Hilo. This event was the largest earthquake to occur on the island in over a century. The tsunami triggered by this earthquake caused two fatalities and widespread damage along the Kalapana coast. The Hawaii Civil Defense Agency estimates that the quake and tsunami caused more than $4 million in damage [*Tilling et al.*, 1976].

Focal mechanisms of the 1975 earthquake and its aftershocks indicate that the event was caused by sudden seaward movement along a subhorizontal fault beneath the south flank [*Ando*, 1979; *Furmamoto and Kovach*, 1979; *Crosson and Endo*, 1982], the region south of Kilauea's two rift zones (Figure 1). The focal mechanisms are consistent with the direction of the coseismic surface displacements determined by trilateration and leveling [*Lipman et al.*, 1985]. The seismic models [*Ando*, 1979; *Furmamoto and Kovach*, 1979; *Crosson and Endo*, 1982] are, however, difficult to reconcile with the 8 m of horizontal surface displacement seen in the trilateration data [*Bürgmann and Delaney*, 1996] since none of them predict such large sur-

face displacements. *Ando*'s [1979] fault model is also inconsistent with the tsunami arrival times and amplitudes [*Ma et al.*, 1999]. *Ma et al.* [1999] were able to explain the tsunami wave arrival times and amplitudes with a combination of faulting and large-scale slumping.

In 1989 a $M6.1$ earthquake again shook Kilauea's south flank. This quake also occurred along a subhorizontal fault, with seaward directed slip [*Chen and Nabelek*, 1990; *Arnadottir et al.*, 1991]. Its epicenter was <10 km from the 1975 $M7.2$ epicenter, but the rupture plane extended eastward from the epicenter, whereas the 1975 earthquake propagated westward. The fault plane geometry inferred from leveling data was several kilometers shallower than the plane defined by the aftershock sequence [*Arnadottir et al.*, 1991]. The anomalous depth of the model fault plane may be an artifact of the homogenous elastic half-space model assumption in what is an undoubtedly complex structure [*Du et al.*, 1994, 1997].

These major earthquakes are generally assumed to occur on the interface between the volcanic edifice and the top of the oceanic plate between 9 and 12 km deep [*Ando*, 1979; *Furmamoto and Kovach*, 1979; *Crosson and Endo*, 1982; *Lipman et al.*, 1985; *Wyss*, 1988; *Arnadottir et al.*, 1991; *Bryan*, 1992]. The depth of the fault, inferred from the larger south flank earthquakes, is consistent with the depth determined by seismic refraction studies [*Zucca and Hill*, 1980]. The dip of this fault is not well constrained, with published estimates ranging from 20° south-southeastward [*Ando*, 1979] to 6° northward [*Got et al.*, 1994]. Several studies favor a slightly north-northwestward dip [*Furmamoto and Kovach*, 1979; *Crosson and Endo*, 1982; *Got et al.*, 1994], consistent with the dip of the seafloor-volcano interface [*Zucca and Hill*, 1980; *Thurber and Gripp*, 1988].
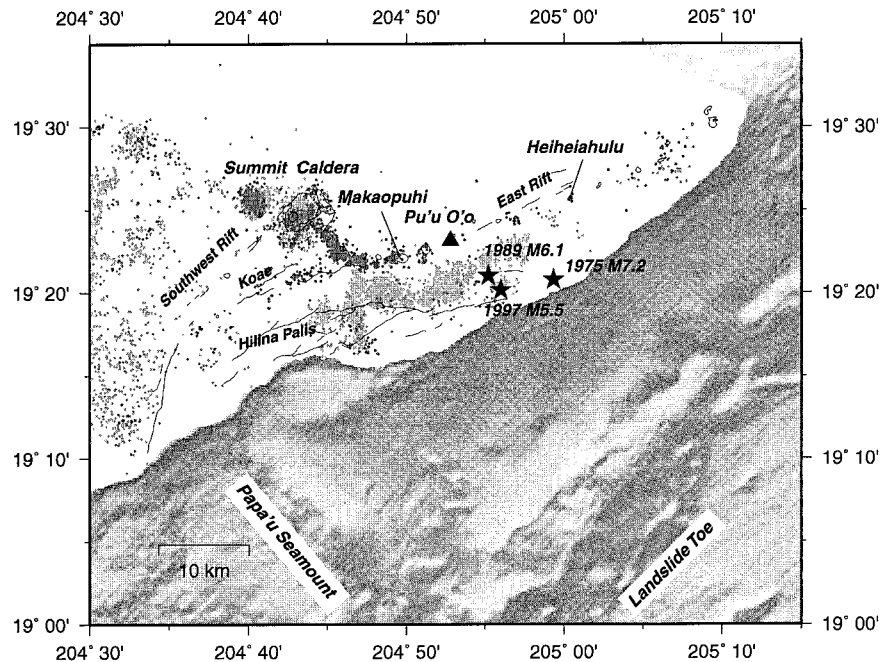
The mechanics of south flank seismicity is not fully understood. Initially, it was hypothesized that the south flank was

---

[1]Now at Department of Earth Sciences, University of Southern California, Los Angeles.

[2]Now at U.S. Geological Survey, Vancouver, Washington.

Figure 1. Map of Kilauea Volcano, showing major geological structures, bathymetry, and epicenters of recent earthquakes. Stars represent epicenters for major earthquakes, and dots represent seismicity between September 1990 and June 1996. The light shaded dots represent quakes that occurred between 5 and 12 km depth. The dark shaded dots represent quakes that occurred between 0 and 5 km depth.

gravitationally unstable and could be considered as a giant landslide [*Stearns and Clark*, 1930]. *Eissler and Kanamori* [1987], interpreting teleseismic surface waves, prefer a landslide interpretation for the 1975 $M7.2$ earthquake, their model being equivalent to a single force rather than a double-couple mechanism. If Kilauea's south flank can be interpreted as a gravity slide, then the rift zones may be passive features, with the magma filling in the void created by the sliding flank. *Dieterich* [1988] demonstrated that long-term stable growth of the rift zones requires that flank slip decrease the normal stresses acting perpendicular to the rift. However, *Dieterich* [1988] also showed that a flank that is constantly sliding away under the force of gravity would not allow for "trapped" dike intrusions, or dike intrusions without surface eruptions, which are common on Kilauea.

Others have suggested forceful intrusion of magma into the rift zone as the mechanism for the 1975 earthquake [*Swanson et al.*, 1976; *Ando*, 1979; *Dvorak et al.*, 1994]. The emplacement of dikes within the rift zone compresses the adjacent flanks, and this compression is relieved by south flank seismicity. According to proponents of this hypothesis the north flank of Kilauea remains relatively stable due to the "buttressing effect" of Mauna Loa. Geodetic, seismic, and geologic data show that in the years prior to the 1975 Kalapana earthquake the south flank underwent rift normal compression and uplift as a result of frequent dike intrusions into the rift system [*Swanson et al.*, 1976]. Prior to the 1989 $M6.1$ earthquake, however, there had been an ongoing eruption in the east rift zone beginning in 1983, with very few intrusions into the rift [*Delaney et al.*, 1993].

A number of scientists have suggested that a deep magma or cumulate body at the base of the rift zone provides the driving force for south flank motion [*Ryan*, 1988; *Delaney et al.*, 1990; *Clague and Denlinger*, 1994; *Borgia*, 1994]. There is geodetic evidence for deep rift dilation [*Delaney et al.*, 1990, 1993; *Owen et al.*, 1995], although the rift zones are aseismic below ~5 km [*Klein et al.*, 1987]. In this model the extension of the deep magma body is caused by magmatic intrusion or by the spreading of dense olivine cumulates under their own weight at the base of the rift [*Clague and Denlinger*, 1994]. In either case, the deep rift expansion is the primary driving force behind south flank motion and seismicity.

These mechanical interpretations of Kilauea Volcano can be evaluated in greater detail with better constraints on the kinematics. Seismic data cannot tell us much about the rates of dilation within the rift zone or slip along the decollement as both phenomena occur largely aseismically. The geometry of the active fault slip and the active rift dilation are crucial for understanding the relative importance of gravitational sliding versus forceful intrusion of magma. In addition, it is important to know the dip of the fault plane and how the actively slipping fault area compares to the rupture planes of prior south flank earthquakes. These are questions we address, using Global Positioning System (GPS) data to constrain the geometry of fault slip and rift opening and giving us a detailed kinematic picture of the volcano.

2. Data

2.1. Network

The GPS measurements presented in this paper have significantly improved the spatial coverage of geodetic measurements on Kilauea. Dense spatial coverage is needed in order to resolve both magmatic and seismic sources of deformation. Many of the stations just north of the rift zone were installed in 1993, and they provide constraints on the deep rift dilation that were not included by *Owen et al.* [1995]. We have repeated GPS measurements for 70 stations on the island of Hawaii
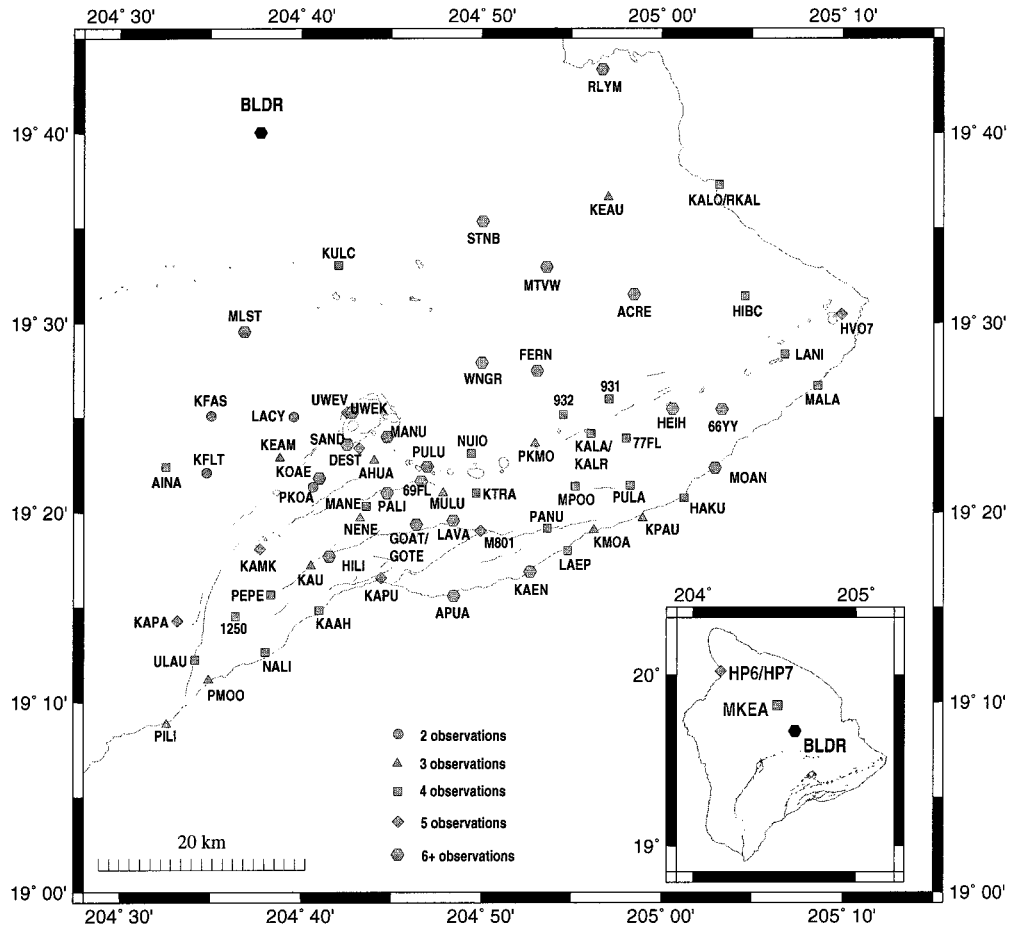
Figure 2. GPS stations surveyed as part of the Kilauea network between 1990 and 1996. BLDR is the reference station for velocity calculations. Stations with two names are stations where the first station was replaced by the second. Inset shows stations surveyed in the far field.

(Figure 2). Descriptions of monumentation and receiver characteristics are given in the appendix.

2.2. Data Analysis

The analysis methods and software used for processing the data have changed over the years. The 1990 and 1992 campaign data were processed using Bernese 3.3 software [*Rothacher et al.*, 1990; *Beutler et al.*, 1988] following the analysis method of *Davis et al.* [1989]. In processing the 1990 and 1992 data, three North American stations were used as fiducial sites in order to improve the satellite orbits and to tie the local network to a global reference frame. The 1990 data analysis used Mojave, California (MOJV); Richmond, Virginia (RICH); and Westford, Massachusetts (WSTF); and the 1992 analysis used Jet Propulsion Laboratory (JPL) Mesa, California (JPLM); Penticton, British Columbia, Canada (PENT); and Algonquin, Ontario, Canada (ALGO). The satellite orbits are well constrained nearest the fiducial stations [*Larson et al.*, 1991], whereas Hawaii is several thousand kilometers outside the fiducial network. To improve the accuracy of the estimated orbital parameters, we processed the data in 4-day orbital arcs. Ambiguity resolution, while not uniformly successful, improved the day-to-day repeatability for those sites with repeated measurements.

The data collected since 1993 were processed using GIPSY/OASIS II software developed at the Jet Propulsion Laboratory

(JPL) [*Zumberge et al.*, 1997; *Gregorius*, 1996]. GIPSY allows for time-dependent estimates of the tropospheric path delay. On Kilauea, where the water content of the troposphere is highly variable, a stochastic parameter updated every epoch should provide a more realistic estimate of the tropospheric zenith delay. Daily solutions were calculated for each campaign from 1993 through 1996. Ambiguity resolution was again used to improve the station position repeatability. All of the data were processed within the International Terrestrial Reference Frame (ITRF) reference frame. The reference frame was established by fixing fiducial sites on North America and Hawaii (1990–1993) or by fixing the orbital parameters and satellite clocks to JPL-generated solutions, calculated within the ITRF reference frame [*Zumberge et al.*, 1997]. The data processing consistently used an elevation cutoff angle of 15°, as different cutoff angles were found to cause shifts in the height estimates.

2.3. Precision

The uncertainties in the station positions calculated by the analysis software underestimate the real errors in the station positions. A simple way to estimate the precision in the positions is to examine the repeatability of station positions within a single survey. A weighted least squares network adjustment was used to calculate the average station position during each campaign, taking into account the full data covariance from the

Table 1. Weighted RMS Values for GPS Campaigns

Campaign	East WRMS	North WRMS	Vertical WRMS
1990 September	10.8	4.5	55.2
1992 March	7.0	3.1	17.0
1993 August	3.6	3.2	13.8
1994 July	2.7	2.5	13.7
1995 June	2.6	2.9	10.2
1995 September	3.6	2.8	9.8
1996 February	2.3	4.2	16.6
1996 April	3.1	2.8	9.7
1996 July	3.0	2.6	14.3

Weighted RMS values are in millimeters.

daily or 4-day solutions. The position covariance matrices were then scaled such that the weighted residual sum of squares divided by the degrees of freedom (hereinafter referred to as the mean square error) in the network adjustment was equal to unity. Table 1 lists the weighted root-mean-square (WRMS) of the adjustment residuals, which are the difference between the observed and mean station positions, for each campaign. The precision of the measurements improved significantly over the first 3 years as the GPS satellite constellation improved, the global network of permanent sites expanded, and receiver quality increased. The introduction of stochastic troposphere estimates likely contributed to the improvement of measurement precision between 1992 and 1993. Since 1993 the WRMS has been approximately the same for each campaign, indicating that the changes in GIPSY processing schemes, while they improved processing efficiency, did not affect local network precision.

2.4. Velocity Estimate: Method and Evaluation

The average velocities between 1990 and 1996 (Figures 3a and 3b and Table 2) were calculated relative to BLDR, a station in the saddle between Mauna Loa and Mauna Kea that is far from active volcanism and seismicity. Stations north and west of the reference station were stable within errors, confirming the stability of BLDR. A weighted least squares estimate, including the full spatial covariance, was used to calculate the velocities for all of the sites simultaneously. We used standard propagation of errors to estimate the velocity covariance. Stations that were replaced by nearby bench marks were constrained to have the same velocity as the new bench marks; only one station velocity from each pair is included in the final velocity solution. Two stations (KALA and HVO7) had corrections added to their station positions. KALR replaced KALA in the 1996 campaign, and the relative position between the two sites was measured at a later date. This offset was subtracted from the KALR position to get the 1996 KALA measurement. A correction was added to the 1993 HVO7 measurement to account for an antenna setup over the wrong centering mark. The correction errors were propagated into the new station position uncertainty.

The mean square error of the velocity estimate, normalized to the a priori data covariance, is 7.3. If the constant velocity model and the data errors were correct, the mean square error should be unity. To understand better the cause of the large misfit in the velocity solution, we looked at the mean square errors in the north, east, and vertical components for each station that had three or more observations. The mean square error for the north component was greater than unity at ~80% of the sites, while the mean square errors of the vertical com-

ponent were less than unity at ~60% of the sites. Sites such as MKPM, HP6, and STNB, which are thought to be in stable regions of the Big Island of Hawaii, had large mean square errors in the north component and low mean square errors in the vertical component. We therefore assumed that improper scaling of the north, east, and vertical components contributed to the misfit of the velocity model. To correct for this improper scaling, we examined the weighted least squares network adjustment for each campaign. For each survey since 1993 the ratio of the north, east, and vertical mean square error to the mean square error for the entire data set was computed. The average ratios were 1.12 for the east component, 1.41 for the north component, and 0.47 for the vertical component. These values were used to scale each station position covariance matrix before it was used in the velocity field calculation. In order to scale the off-diagonal terms appropriately the covariance matrix was first converted into a correlation matrix. Then the north, east, and vertical terms along the diagonal of the correlation matrix were scaled by the above scaling factors. Finally, the scaled correlation matrix was converted back to the covariance matrix. After applying this scaling, the mean square error for the velocity estimate was reduced to 5.6. There were still more sites that had mean square errors above unity in the horizontal than the vertical, but this imbalance is more likely due to true variations in the displacement rates.

A total of 32 velocity components from 24 stations has mean square errors that are >95% confidence limit for fitting the linear model. With 73 station velocities, each with three velocity components, we expect only 11 components to fall outside the 95% confidence interval. Either we have underestimated the position errors, or the steady state model is invalid. If a station's velocity varies with time, nearby sites would likely have similar velocity variations and so also have high mean square errors. Indeed, of the 24 stations that did not fit the linear model, 3 were at the summit, 5 were clustered in the lower southwest rift, 7 were grouped around MPOO near the east rift, and 6 were concentrated between the Hilina faults and the coast. The time series of the stations in these regions were examined for significant rate changes, and we found temporal variations that may be real. This is a subject of ongoing study.

2.5. Velocity Estimate: Results

The horizontal velocities (Figure 3a) show rapid seaward displacement of the south flank, consistent with previous geodetic studies [*Delaney et al.*, 1993; *Owen et al.*, 1995; *Delaney et al.*, 1998]. The highest velocities occur along the coast and just north of the Hilina faults. West of KAPU and east of KMOA, there is a significant decrease in station displacement rates that continues to the distal ends of the south flank. The decrease in velocity on the eastern and western ends roughly correlates with the edge of the Hilina fault system. The gradients in the velocities from east to west show where shear strain is accumulating within the south flank. There is no surficial evidence for tear faulting in these regions. The lack of tear fault structures could imply that this pattern of deformation is not sustained over long time periods and that the western and eastern ends will eventually catch up, perhaps in seismic events. Alternatively, recent lava flows might have covered up any fault structures.

There is a dramatic decrease in velocities between stations just north of the east rift zone (931, 932, NUIO and PKMO) and stations on the north flank (WNGR and FERN). In the
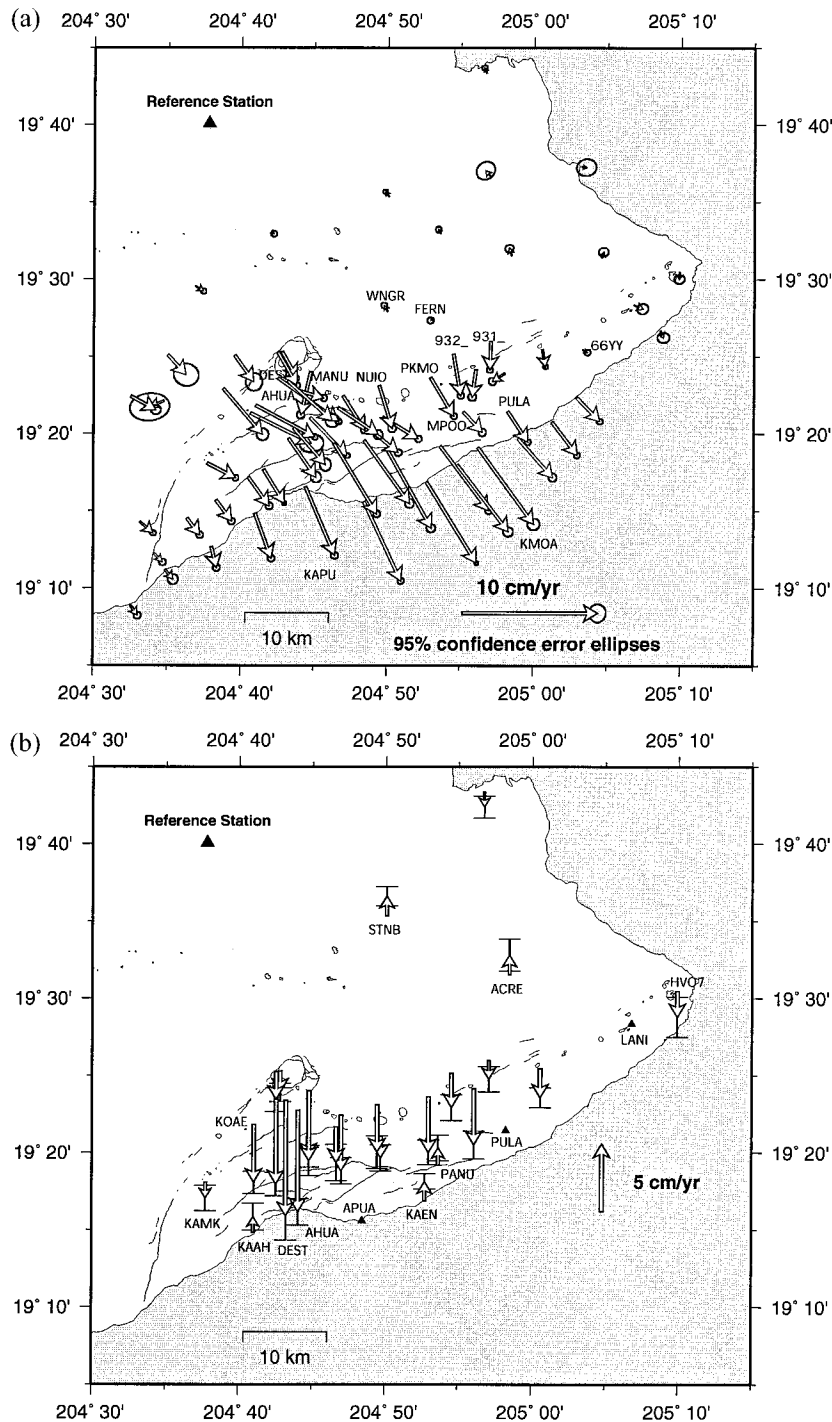
Figure 3. (a) Average horizontal velocities for 1990–1996; (b) Average vertical velocities. Both plots show velocities relative to BLDR; error bars in Figure 3b are 2-sigma errors. Only stations with vertical velocities above the 2-sigma error are shown in Figure 3b.

region north of MPOO the pattern of extension across the rift is reversed. There is compression across the rift and extension between the stations in the midflank and the coast.

The velocity pattern around the summit is clearly influenced by a local source of deformation displacing AHUA and MANU toward a point a few kilometers south of the summit caldera. This pattern is consistent with deflation of a magma chamber near the summit caldera. The region bounded by the summit, the two rift zones, and the Koae Fault zone is under-

going steady subsidence, with the peak subsidence occurring just south of the summit caldera region (-8.53 ± 0.90 cm/yr at DEST; -7.51 ± 0.49 cm/yr at AHUA) (Figure 3b). Subsidence is also observed along the east rift zone possibly as far downrift as HVO7. LANI is the only site that lies within the surface expression of the east rift zone that does not show a significant subsidence rate. The subsidence rate measured at LANI, -0.18 ± 0.76 cm/yr, is consistent at the 2-sigma level with the subsidence measured at its nearest east rift zone neighbor,

Table 2. The 1990–1996 Average Velocities

Station	Longitude	Latitude	East	±	North	±	Up	±
1250	−155.3937	19.2419	0.94	0.11	−1.24	0.10	0.07	0.47
66YY	−154.9446	19.4238	0.36	0.10	−0.19	0.09	0.07	0.46
69FL	−155.2227	19.3608	2.98	0.14	−1.97	0.14	−2.64	0.66
77FL	−155.0328	19.3987	−0.92	0.11	−0.61	0.11	−0.62	0.56
931_	−155.0487	19.4330	−0.07	0.10	−2.12	0.09	−1.40	0.46
932_	−155.0913	19.4191	0.54	0.10	−3.08	0.10	−2.53	0.48
ACRE	−155.0257	19.5252	−0.18	0.13	0.56	0.11	1.47	0.59
AHUA	−155.2661	19.3791	1.77	0.10	−0.53	0.10	−7.51	0.49
AINA	−155.4580	19.3733	1.83	0.15	−1.01	0.13	−0.33	0.72
APUA	−155.1926	19.2599	2.75	0.10	−5.84	0.09	0.27	0.52
DEST	−155.2800	19.3897	3.30	0.21	−2.92	0.20	−8.53	0.90
FERN	−155.1153	19.4581	−0.16	0.10	−0.18	0.09	−0.27	0.49
GOTE	−155.2270	19.3226	3.17	0.11	−5.20	0.11	1.00	0.53
HAKU	−154.9791	19.3459	1.87	0.09	−2.45	0.09	0.59	0.45
HEIH	−154.9902	19.4242	0.23	0.08	−1.27	0.07	−2.17	0.36
HIBC	−154.9233	19.5235	0.13	0.15	0.42	0.13	−0.36	0.67
HILI	−155.3073	19.2945	1.53	0.07	−2.49	0.06	0.56	0.32
HP7_	−155.8207	20.0268	0.08	0.18	−0.08	0.16	−0.50	0.82
HVO7	−154.8346	19.5078	−0.04	0.16	−0.51	0.13	−1.93	0.74
KAAH	−155.3168	19.2471	1.21	0.10	−3.31	0.10	1.16	0.50
KAEN	−155.1215	19.2812	3.72	0.06	−5.98	0.06	1.44	0.28
KALA	−155.0656	19.4026	−0.28	0.12	−2.05	0.11	−4.17	0.52
KAMK	−155.3713	19.3010	2.09	0.09	−1.08	0.09	−1.16	0.46
KAPA	−155.4472	19.2378	0.97	0.09	−0.84	0.08	−0.02	0.41
KAPU	−155.2596	19.2757	2.19	0.12	−5.06	0.10	0.67	0.56
KAU_	−155.3244	19.2862	1.54	0.11	−2.12	0.11	0.24	0.54
KEAM	−155.3532	19.3814	2.90	0.18	−3.37	0.18	−0.62	0.90
KEAU	−155.0498	19.6105	−0.38	0.28	0.47	0.27	1.16	1.43
KFAS	−155.4163	19.4180	1.34	0.37	−1.48	0.34	−1.84	1.58
KFLT	−155.4206	19.3682	−1.04	0.59	−0.46	0.42	2.63	5.08
KMOA	−155.0629	19.3180	4.14	0.18	−5.64	0.17	0.98	0.95
KOAE	−155.3165	19.3633	4.40	0.09	−2.34	0.08	−4.28	0.40
KPAU	−155.0175	19.3281	2.57	0.12	−2.88	0.13	0.66	0.63
KTRA	−155.1717	19.3505	2.64	0.10	−1.58	0.10	−1.60	0.48
KULC	−155.2992	19.5508	0.16	0.09	−0.13	0.09	0.35	0.45
LACY	−155.3403	19.4174	1.41	0.25	−1.96	0.27	−0.41	1.30
LAEP	−155.0868	19.2997	3.81	0.15	−4.94	0.14	1.29	0.70
LANI	−154.8868	19.4725	0.66	0.17	−0.29	0.16	−0.18	0.76
LAVA	−155.1929	19.3261	3.38	0.14	−4.67	0.14	0.49	0.65
M801	−155.1674	19.3170	3.34	0.14	−5.87	0.12	−0.65	0.63
MALA	−154.8563	19.4447	0.20	0.18	−0.51	0.16	−0.76	0.76
MANE	−155.2733	19.3391	2.37	0.17	−2.70	0.19	0.74	0.82
MANU	−155.2541	19.3998	−0.73	0.12	−3.19	0.12	−5.16	0.56
MKEA	−155.4810	19.8228	0.13	0.08	0.15	0.08	−0.06	0.40
MLST	−155.3857	19.4924	0.61	0.09	−0.38	0.08	0.43	0.40
MOAN	−154.9508	19.3724	1.69	0.09	−1.76	0.08	0.85	0.44
MPOO	−155.0799	19.3564	1.41	0.12	−1.49	0.11	−0.52	0.56
MTVW	−155.1065	19.5490	−0.16	0.09	0.31	0.09	−0.26	0.47
MULU	−155.2025	19.3504	3.16	0.11	−2.57	0.11	−0.70	0.52
NALI	−155.3662	19.2109	0.38	0.11	−1.55	0.10	0.76	0.47
NENE	−155.2788	19.3281	2.04	0.16	−2.87	0.16	−1.21	0.78
NUIO	−155.1761	19.3851	0.98	0.12	−3.16	0.12	−3.49	0.60
PALI	−155.2542	19.3505	2.76	0.08	−2.82	0.07	−1.51	0.35
PANU	−155.1059	19.3196	3.60	0.10	−4.74	0.10	1.30	0.47
PEPE	−155.3612	19.2611	1.15	0.11	−1.54	0.10	−0.52	0.50
PILI	−155.4574	19.1475	0.50	0.11	−0.73	0.11	0.14	0.51
PKMO	−155.1172	19.3938	1.73	0.10	−2.86	0.09	−4.12	0.46
PKOA	−155.3224	19.3554	4.53	0.37	−2.23	0.28	−3.04	2.54
PMOO	−155.4185	19.1862	0.58	0.15	−0.71	0.15	−0.93	0.73
PULA	−155.0292	19.3570	1.49	0.09	−2.24	0.09	0.43	0.46
PULU	−155.2170	19.3736	1.60	0.11	−2.52	0.11	−4.12	0.50
RKAL	−154.9464	19.6218	0.36	0.30	−0.06	0.25	−1.35	1.25
RLYM	−155.0548	19.7227	−0.15	0.09	0.37	0.08	−1.11	0.41
SAND	−155.2914	19.3929	4.51	0.09	−3.21	0.09	−6.44	0.43
STNB	−155.1658	19.5889	−0.27	0.07	0.38	0.07	1.45	0.36
ULAU	−155.4307	19.2038	0.60	0.11	−0.64	0.10	0.55	0.49
UWEK	−155.2868	19.4211	1.11	0.07	−1.93	0.07	−1.57	0.34
UWEV	−155.2911	19.4209	1.40	0.09	−2.43	0.09	−2.07	0.44
WNGR	−155.1667	19.4651	−0.26	0.09	0.44	0.09	−0.19	0.44

Average velocities are in centimeters per year, with 1-sigma errors.

HVO7. The majority of stations within and near the surface expression of the southwest rift zone are not subsiding at a measurable rate. The exceptions are the stations just south of the southwest rift and north of the Koae normal faults, KAMK and KOAE.

Three stations near the coast show significant uplift: KAEN (1.44 ± 0.28 cm/yr), KAAH (1.16 ± 0.47 cm/yr), and PANU (1.30 ± 0.50 cm/yr). The slight uplift measured at the coast is consistent with geodetic surveys since the 1975 earthquake [*Delaney et al.*, 1993]. *Dvorak et al.* [1994] and *Delaney et al.* [1998] see a decline in uplift rate between 1975 and the mid-1980s. We do not see a decline in uplift rate in the GPS data since 1990, but the rate decrease between 1975 and the mid-1980s as measured from well and tide gauge data was very small (~0.3 cm/yr). GPS sites near the tide gauge (APUA) and well site (PULA) do not show significant uplift. The vertical velocity at APUA, 0.27 ± 0.52, cm/yr, is barely consistent with the rate measured at the Apua tide gauge, 2.1 ± 0.4 cm/yr at the 2-sigma level. *Delaney et al.* [1993] report −1.2 ± 2.6 cm/yr of subsidence at the Pulama well starting in the mid-1980s; the uplift rate at the PULA GPS site is 0.43 ± 0.46 cm/yr, which is again consistent with the older data at the 2-sigma level. Prior to the 1975 earthquake, uplift along the south flank was greatest close to the rift zone, not along the coast. This change in uplift rates might be consistent with a change in the pattern of slip along the decollement. The current pattern of vertical flank velocities is also different from the 1975 coseismic displacements, which included significant subsidence along the coast.

The slow rates of uplift at stations along the coast (KAEN and KAAH) and within the south flank (PANU) are likely the result of broad deformation patterns on Kilauea. The uplift rates at stations far from the rift on the north flank (ACRE and STNB) are not observed at other stations north of the rift and are probably not significant.

3. Model

Kilauea has numerous possible sources of deformation, including rift zones, magma storage chambers, normal faults, and a subhorizontal decollement. Because of the complexity of the system, GPS data alone cannot uniquely determine the geometry of the active deformation sources. We therefore place some constraints on the geometric parameters such that the estimated models will be consistent with geologic and seismic data as well as the geodetic data. The observations are modeled with simple dislocations in a homogeneous elastic half-space [e.g., *Okada*, 1985] and point sources of volume change [*Mogi*, 1958]. The half-space approximation is appropriate for Kilauea since the volcano has gently sloping topography. The 3.3° average topographic slope of Kilauea's south flank [*Moore and Mark*, 1992] is taken into account by subtracting this value from the estimated dip parameter.

The GPS data cannot be fit with only slip along a decollement or only opening along the rift system because of the steep north-south gradient in velocity across the east rift zone. This gradient is especially evident between stations just north of the middle east rift (PKMO, 932, 931, and NUIO) and stations just 5 km farther north (FERN and WNGR). If only slip occurred along a decollement, fault slip rates sufficient to fit the observed horizontal velocities along the coast would misfit data on the north flank (Figure 4a). Similarly, the amount of rift opening necessary to fit observed horizontal velocities on the south flank would cause significant northward motion on the

north flank (Figure 4b). Slip along a shallow decollement could fit the gradient across the rift zone only if the fault is <3 km deep, which is inconsistent with the depth of the larger south flank earthquakes [*Klein et al.*, 1987]. The data require both fault slip along a decollement and rift opening, which effectively decouples the south flank from the north flank.

The surface displacements are nonlinear functions of the source geometry. In order to search systematically for the best fitting geometry we use a nonlinear optimization algorithm. Since the parameter space has multiple broad local minima, derivative-based optimization algorithms are not ideal for this problem. Instead, we use random cost methods [*Berg*, 1993; *Murray et al.*, 1996] that are designed to avoid getting trapped in local minima.

Extensive forward modeling, plus several preliminary optimization searches allowed us to narrow the search for the optimal parameters. A total of four dislocation planes and one point source of volume change were used to approximate the important sources of deformation. Two dislocation planes were used to model the decollement, and two dislocation planes were used to model the rift zone east of the summit caldera. Preliminary modeling showed that the addition of a point source of volume change at the summit significantly improved the fit to data in the near-summit region. Preliminary modeling also showed that dislocation planes approximating the southwest rift zone did not improve the data fit. This result is consistent with the very small number of earthquakes in the southwest rift zone between 1990 and 1996. While we do observe subsidence at KOAE and KAMK (Figure 3b), this deformation can be explained with seaward slip along the decollement.

Initial modeling estimated the slip and opening rates on the fault and rifts separately. However, the rift opening rates were often significantly greater than the estimated fault slip rates, which is difficult to justify kinematically. Therefore, in the parameterization of the final search the east rift opening and the east fault slip rate were constrained to be equal. The west fault slip rate was constrained to be equal to the vector sum of the left-lateral strike-slip rate and the rift opening rate across the upper east rift. The fault slip and opening rates, along with the source geometry, were estimated, using the random cost search method even though the surface displacements are linear functions of the slip and opening rates.

The bounds on the model parameters were chosen to be geologically and geophysically reasonable. The two fault planes were constrained to have the same strike, dip, and depth so that they approximated a single fault plane at depth. The east rift plane was constrained to have the same strike as the fault planes. The two rift planes were forced to meet at the bend in the rift zone near Makaopuhi Crater. The east rift plane was constrained to lie within the surface expression of the rift, but the upper east rift plane was allowed to be anywhere within the surface expression of the rift zone and the Koae fault system. The rift plane dips were fixed to 90°, and the rift planes were not allowed to extend below the fault planes.

For most of the model parameters these bounds were also sufficient to span the range of values that fit the data well. The surface projection and rates of motion for the dislocation planes in the best fitting model are shown in Figure 5. The mean square error for the best fitting model is 19.3, implying there is still unmodeled signal, yet the model reduces the data variance by 95%. Figures 6a and 6b plot the observed and model-predicted vectors for comparison.
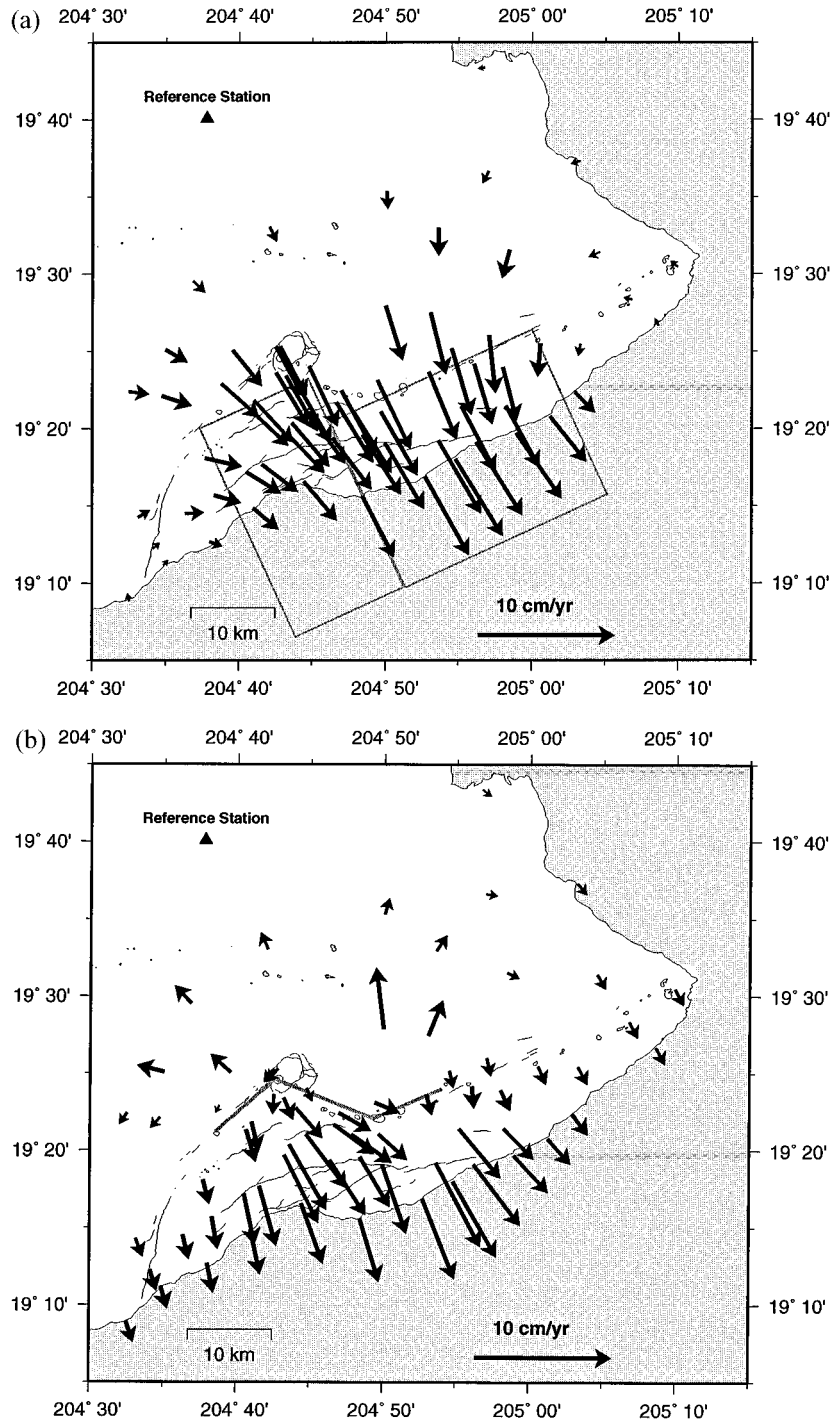
Figure 4. (a) Model predicted velocities for a decollement-only model. The shaded rectangles are the surface projection of the fault planes. The model fault plane is dipping 7° north-northwestward and is at 9 km depth. When fault slip rates are chosen to fit the rates along the south coast, stations on the north flank show significant southward motion not observed in the GPS measurements. (b) Model predicted velocities for a rift-opening-only model. The rift planes extend from 3 to 9 km depth.

To determine how well the data resolves the model parameters, the mean square error is plotted as a function of model parameters in Figures 7–10. We let all parameters vary simultaneously to get a more realistic estimate of the model values that fit the data well but still imposed the same constraints on the model parameters as described above. It should be noted that there are also correlations between many of the parameters that are not shown in the figures. In this paper, we used over 2,000,000 models to find the minimum mean square error versus model parameter curve for each parameter. In order to smooth between the discrete model parameter values that were tested, the parameter's range was divided into 20 equal intervals. The minimum mean square error was found for each interval. Since the parameter space was not evenly searched,
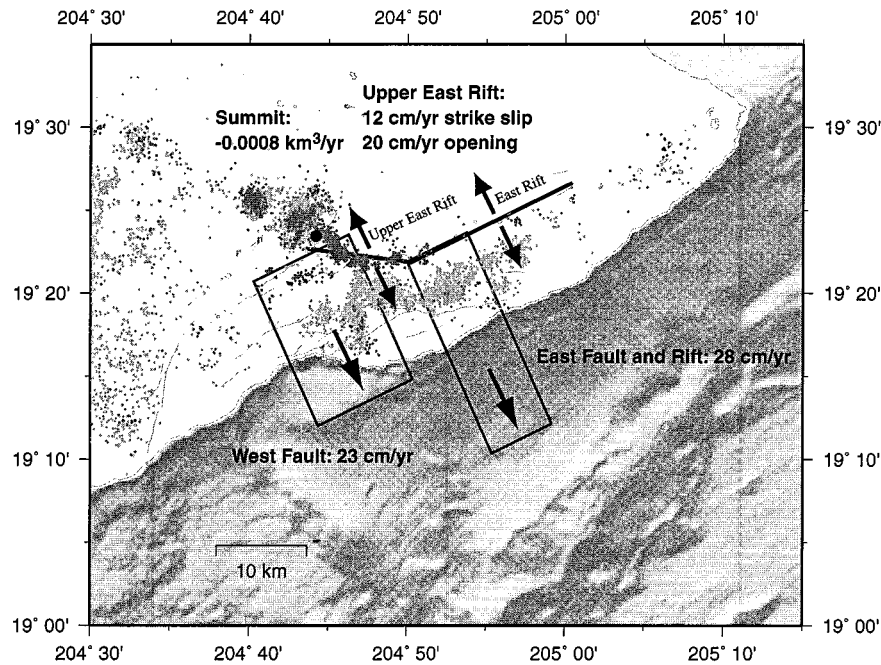
Figure 5. The location of the best fitting model dislocations, summit point source, and seismicity from September 1990 to June 1996. The light shaded dots represent quakes that occurred between 5 and 12 km depth. The dark shaded dots represent quakes that occurred between 0 and 5 km depth. The rectangles and lines are the surface projections of the model fault and rift dislocations, respectively. The solid circle shows the location of the point source of volume change in the summit region. The estimated slip rates for these dislocations are indicated. Vectors show the direction of fault slip and rift opening.

some parameters have plots that are not smoothly varying, especially at higher mean square errors. All of the plots vary smoothly near the minimum (or minima) since that is where the most models were generated as the search converged on the best fitting model. If a parameter is well resolved, it will have a narrow range of parameter values for which the model misfit is near the minimum. The dashed lines on Figures 7–10 give a 95% confidence bound on the parameters using the F statistic [*Arnadottir and Segall*, 1994; *Murray et al.*, 1996]. At this value, models have a 5% probability of fitting the data as well as the best fitting model. The F statistic is valid for problems where the models are linear and the data errors are normally distributed. The model here is not linear, and the data errors are not necessarily normally distributed. In estimating fault parameters from geodetic data, confidence bounds on parameters calculated using the F statistic are typically optimistic [*Arnadottir and Segall*, 1994; P. Cervelli et al., Estimating deformation source parameters from geodetic data, submitted to *Journal of Geophysical Research*, 2000.].

The optimal model (Figure 6a) fits the horizontal velocities along the coast and the velocity gradient across the east rift zone reasonably well. The model also matches the change in the orientation of the velocity vectors across the Hilina Pali. However, the tapering displacements at the western end of the flank and the middle east rift zone deformation near MPOO are not adequately fit. KFLT, located north of the southwest rift, has the largest misfit, but it also has the largest error ellipse in the network. The model overpredicts the uplift at KAEN (Figure 6b) but fits the summit and upper east rift zone subsidence well. The subsidence rates in the lower east rift zone (KALA, HEIH, and HVO7) are all underfit by the model.

The range of model parameter values defined by the 95% confidence interval usually falls within the a priori upper and lower bounds; however, there were some parameters that fit the model reasonably well even at these bounds. Models with fault and rift depths at the upper bound of 12 km fit the data well (Figures 7c and 8c). The upper bound was kept at 12 km, since geophysical studies have shown that it is unlikely that the decollement is much deeper than 12 km [*Zucca and Hill*, 1980]. The upper limit of the along-strike length of the east rift is 50 km. While the mean square error is relatively low for a rift that is 50 km long (Figure 8a), at 50 km the rift extends ~10 km offshore, and the mean square error does not change with increasing rift length as there are no data beyond this point. The offshore extent, or width, of the east fault also fits the data reasonably well for values that extend the fault beyond the region covered by the GPS network (Figure 7a). The upper bound is 70 km, which puts the edge of the fault plane ~50 km offshore. The length, or along-strike dimension, of the east fault fits the data well at its lower bound of 3 km, but it is impractical to allow the dimension to be <3 km since the slip rate becomes unreasonably large. The same logic applies to the length of the west fault.

4. Discussion

In order to understand the implications of this kinematic model we compare the best fitting model with geologic structures and microseismicity (Figure 5). As expected from the surface displacement rates, the eastern edge of the east fault plane is approximately coincident with the eastern edge of the Hilina fault system. The western edge of the west fault plane, however, does not correlate precisely with the western edge of
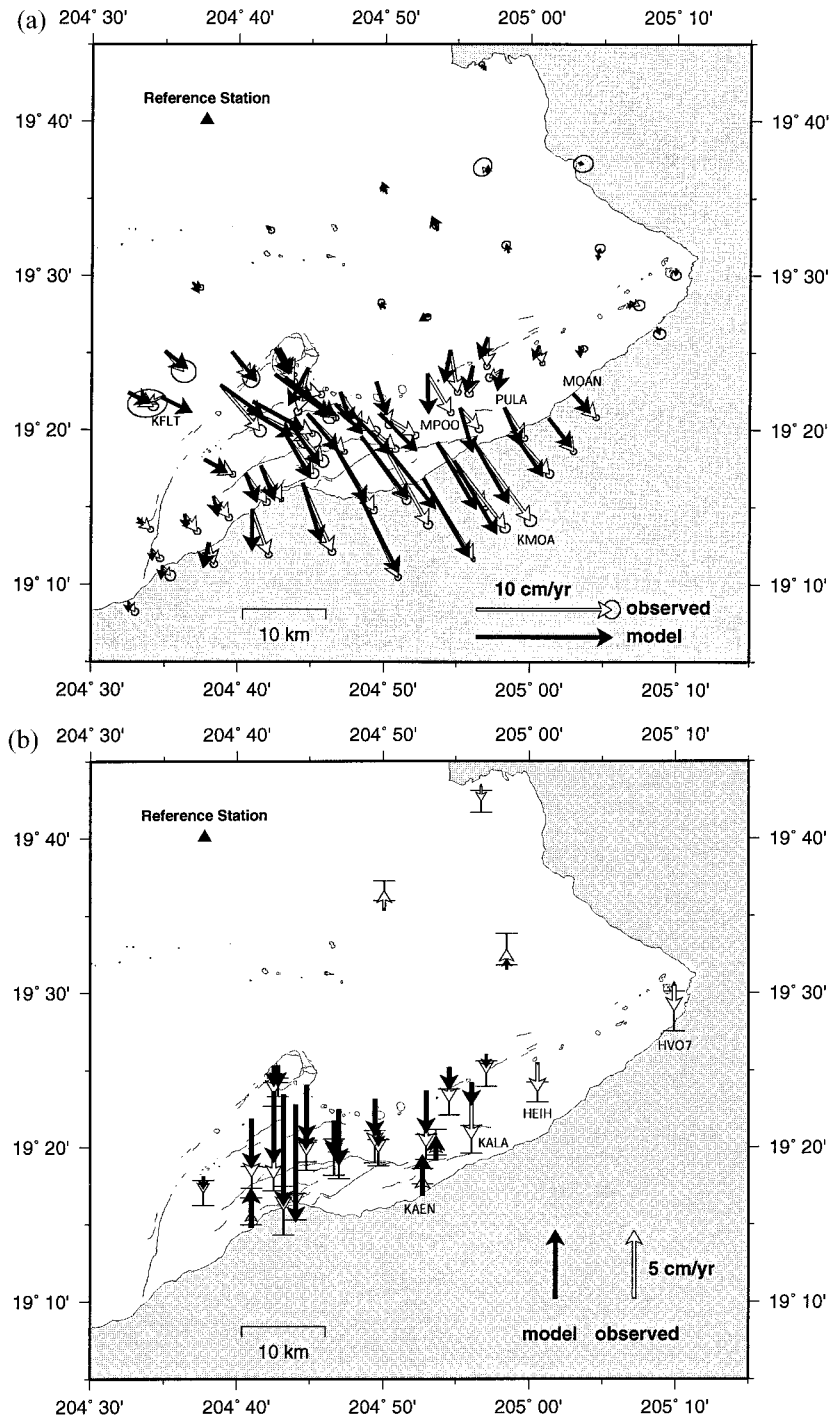
Figure 6. (a) Model and observed horizontal velocities. (b) Model and observed vertical velocities. Figure 6b shows only those stations with vertical velocities above the 2-sigma error.

the Hilina faults. The Hilina fault system sits above the most actively slipping region. However, it should be noted that fault slip extends north of where the Hilina faults would merge with the decollement if they were to extend to that depth.

The west fault length can range from the lower bound value of 8 km up to ~30 km (Figure 7b). This range of fault lengths is greater than the range for the east fault, allowing the west fault to span the central section of the south flank and extend slightly westward beyond the main concentration of microseismicity. It is possible that the geometry of the slipping region is

complex, and while there is a gap in the active fault slip between the east and west faults, this discontinuity is not well resolved. Certainly, given the range of acceptable fault lengths for the west fault (Figure 7), the fault plane can be extended to cover this gap without seriously misfitting the geodetic data. Indeed, the separation into two faults is an artifact of using rectangular dislocations to model a complex fault geometry. The distribution of the fault slip, as well as the rift opening, is more rigorously evaluated using distributed slip inversions [*Owen et al.*, 1998; S. Owen and P. Segall, manuscript in prep-

Fault Geometry
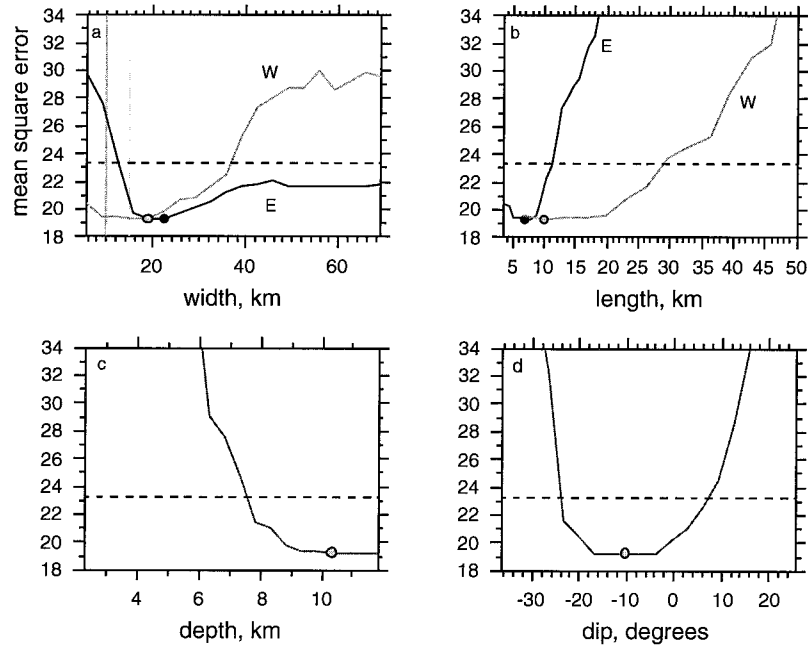
Figure 7. Misfit versus model parameters for the east (dark shaded lines) and west (light shaded lines) fault planes. The dashed line represents the 95% confidence level value. In Figure 7a the darker shaded vertical line marks the approximate location of the coast for the east fault plane, and the lighter shaded vertical line marks the approximate location of the coast for the west fault plane. Negative dips correspond to fault planes dipping islandward or to the north-northwest. Circles mark the best fitting values.

Rift Geometry
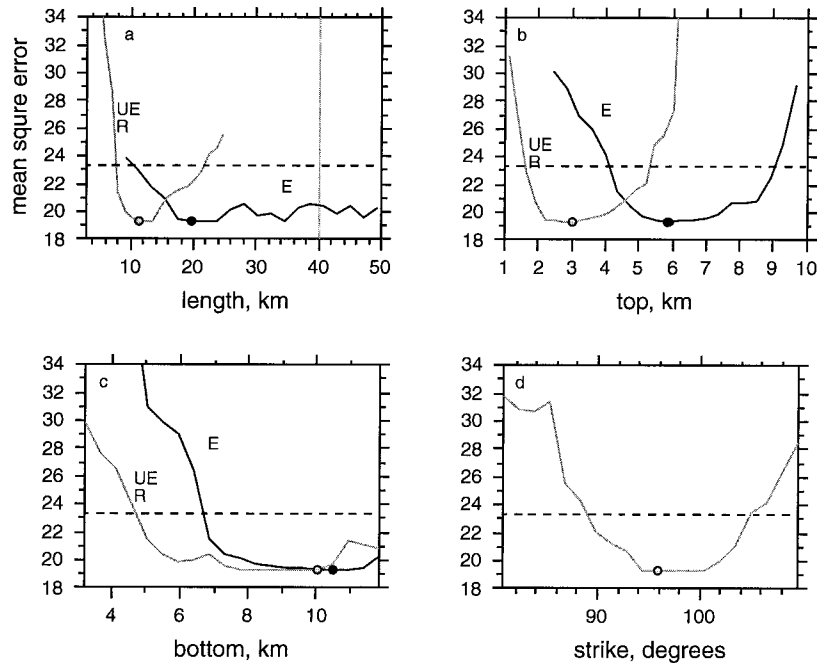
Figure 8. Misfit versus model parameters for the east (dark shaded lines) and upper east rift plane (light shaded lines). The dashed line represents the 95% confidence level. In Figure 8a the vertical line marks the approximate location of the coast. "Top" and "bottom" refer to the top and bottom edge of the rift plane with respect to the free surface. Circles mark the best fitting values.
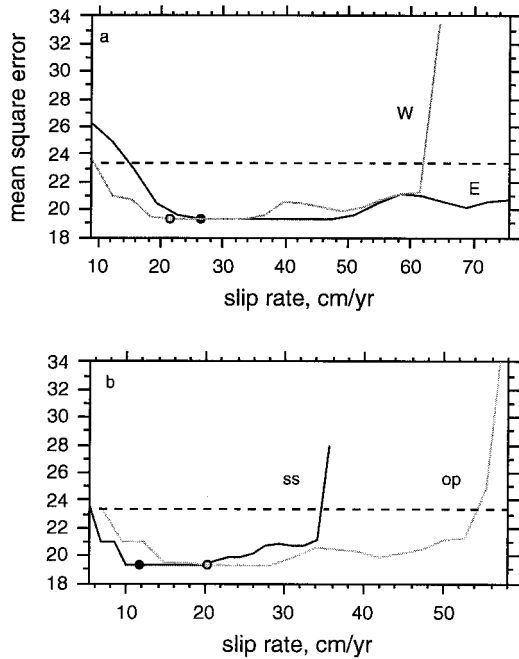
Figure 9. Misfit versus estimated slip rates for the model fault planes. The dashed line represents the 95% confidence level. (a) East rift opening and fault slip rate (dark shaded line) and west fault slip rate (light shaded line). (b) Strike-slip rate (dark shaded line) and opening rate (light shaded line) for the upper east rift plane, where positive slip rates correspond to left-lateral slip across the rift plane. Circles mark the best fitting values.
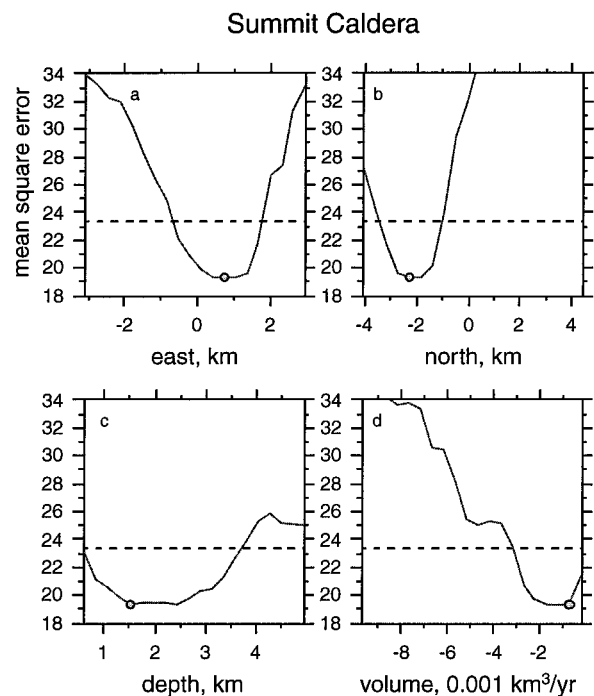
occurred along a section of the decollement predominantly east of the 1975 rupture plane, and yet the 1989 earthquake does not appear to have caused aseismic slip along its rupture plane for years following the earthquake. In addition, *Delaney et al.* [1998] see significant decrease in surface deformation rates after the January 1983 dike intrusion, indicating that the deformation is also responding to the intrusion and ongoing eruption. With the installation of a continuous GPS network on Kilauea [*Lisowski et al.*, 1996] the spatial and temporal evolution of this actively slipping region will be monitored with greater precision.

The east rift plane extends to Heiheiahulu, ~12 km east of the eastern fault and ~15 km downrift of Puʻu Oʻo. It would be difficult to fit the data well with a rift plane that extended <10 km from Makaopuhi (Figure 8), which is still downrift of Puʻu Oʻo and is an area of low seismicity. However, there is also no evidence in this part of the rift zone for shear strain across the deep rift, as is observed along the upper east rift, or shallow magma transport, both of which have been considered mechanisms for rift seismicity [*Gillard et al.*, 1996; *Klein et al.*, 1987].

The western extent of the upper east rift plane ends directly beneath the summit caldera. The preferred strike for the upper east rift plane falls between the Koae fault zone and the surface expression of the rift. Although the station coverage is good near the upper east rift, the data poorly constrain the strike of the rift. The strike ranges between ~90° and 102° (Figure 8d), where a strike of 90° would place the rift plane along the Koae fault system and a strike of 102° would place the rift plane along the surface expression of the upper east rift. This may indicate that actual opening at depth occurs over a broad region between the Koae faults and the upper east rift,

aration, 2000]. These distributed slip inversions show that the data can be fit with a continuous distribution of slip along the decollement without a gap between the east and west faults. Both fault planes extend offshore, at least several kilometers in the rift-perpendicular direction, beyond the zone of active seismicity. The width, or rift-perpendicular dimension, clearly requires that the east fault extends offshore in order to fit the data (Figure 7a). All of the east fault width values that fit the data reasonably well extend beyond the region of active microseismicity. The west fault plane length also extends beyond the region of active microseismicity, although it is not required to extend past the subaerial portion of the south flank. Unlike the east fault, the model misfit increases significantly as the fault plane extends farther offshore.

These results show that the active slipping region is not constrained to the region experiencing active microseismicity and that sections of the fault are creeping with essentially no brittle failure. These sections, however, coincide with the rupture area of the 1975 *M*7.2 earthquake. The 1975 rupture plane is thought to have extended farther offshore than the actively slipping region shown in Figure 5 [*Ma et al.*, 1999]. The coastal subsidence observed in the 1975 earthquake, as compared to the current coastal uplift, would suggest that the coseismic slip extended farther offshore than the currently slipping zone. However, the coastal subsidence in 1975 could also be due to coseismic slip on the Hilina normal faults. It remains to be seen if the current aseismic creep is a postseismic response to the 1975 earthquake [*Dvorak et al.*, 1994], perhaps caused by the earthquake temporarily changing the frictional properties of the fault. However, the 1989 *M*6.1 earthquake

Figure 10. Misfit versus model parameters for the summit point source of volume change. The dashed line represents the 95% confidence level. For Figures 10a and 10b the origin for the north and east coordinates is approximately the center of the summit caldera. Circles mark the best fitting values.

consistent with the model described by *Clague and Denlinger* [1994] and not along a single rift plane. The fault dip has a broad minimum centered at ~10° NNW (Figure 7). The majority of the acceptable values have the fault dipping islandward. The data rule out seaward dips >8°, which is inconsistent with the 20° dip found by *Ando* [1979] for the M7.2 1975 Kalapana quake rupture plane. However, other studies of the 1975 M7.2 quake [*Furmamoto and Kovach*, 1979; *Crosson and Endo*, 1982], microseismicity [*Got et al.*, 1994], and flexure analysis [*Thurber and Gripp*, 1988] have argued that the decollement is dipping islandward, which is consistent with our results. The estimated fault plane depth (Figure 7c) is consistent with the focal depths of the largest south flank earthquakes [*Ando*, 1979; *Furmamoto and Kovach*, 1979] and falls within the range of current microseismicity but is inconsistent with the shallow faulting suggested by *Dvorak et al.* [1994].

The depth of the bottom edge of the rift zone follows a pattern similar to the depth of the east fault (Figure 8). Indeed, since the bottom edge of the rift was not allowed to extend below the fault, this parameter is not completely independent and is highly correlated with fault depth. The range of acceptable values is thus nearly the same as for the fault. As is the case for the best fitting model, it is likely that all models that fit the data well have the rift extending to the fault. The top of the east rift plane does not extend very close to the surface. The previous studies had the top of the rift plane at ~3 km [*Delaney et al.*, 1993; *Owen et al.*, 1995]. However, the model misfits the newer data if the rift extends above ~4 km depth. The top edge of the rift plane in this study is slightly deeper than the 3–4 km depth one would infer from the precisely relocated microseismicity of *Rubin et al.* [1998]. However, the present uniform slip dislocation model does not allow the opening to taper toward the surface. *Rubin et al.* [1998] also analyzed microseismicity from 1980 to 1985, so the time periods of the two studies do not overlap.

The top of the upper east rift is estimated to be shallower than the middle east rift (Figure 8b). In the upper east rift the top edge of the rift can extend to almost 1.5 km depth, although values between 2 and 3.5 km depth fit the data best. The top edge of the rift plane cannot be deeper than ~5.5 km. This finding is consistent with *Gillard et al.*'s [1996] analysis of upper east rift zone seismicity from 1991. In their study the swarm of shallow seismicity in the shallow upper east rift was precisely relocated and found to form very narrow linear bands at ~3 km depth. They were able to explain this seismicity as the result of deep dilation and shear, which create stresses large enough for strike-slip faulting on a vertical plane above the deep rift body.

The estimated fault slip and rift opening rates are high, between 20 and 28 cm/yr. The fault slip rates are similar to those found by *Owen et al.* [1995] and *Delaney et al.* [1993], which were 20 and 25 cm/yr, respectively. The model predicts 0.045 km³/yr of volume increase in the rift zones, less than what was found by *Owen et al.* [1995] (0.06 km³/yr) and greater than the rate estimated by *Delaney et al.* [1993] (~0.025 km³/yr). The model of *Owen et al.* [1995] included significant opening in the southwest rift zone, which accounts for some of the discrepancy between the 1990–1993 opening rates and the 1990–1996 opening rates in this paper. The model geometry presented by *Owen et al.* [1995] was found by using forward modeling, and so the discrepancy between the models in the southwest rift may be the result of the different time periods or the more thorough inversion presented in this paper. The

left-lateral fault slip rate estimated for the upper east rift plane is 12 cm/yr, less than half the 26 cm/yr estimated by *Delaney et al.* [1993] for the 1983 to 1991 time period. It should be noted that the fault slip, rift opening, and rift left-lateral slip rates are not tightly constrained by the data, as can be seen in Figure 9a. The rates found for the best fitting model are all at the lower end of the range of acceptable values. Also, fault slip is not likely to be spatially uniform.

The location and depth of the summit volume point source are consistent with seismic tomography studies [*Thurber*, 1984; *Rowan and Clayton*, 1993] and previous geodetic studies, some including much more data from the summit trilateration and leveling networks [*Swanson et al.*, 1976; *Yang et al.*, 1992; *Wallace and Delaney*, 1995]. We can see from the north-south coordinate that the point source is constrained to be south of the summit caldera (Figure 10). The depth is not as well defined and ranges from 0.5 to ~3.5 km depth. The depth of the point source is strongly correlated with both the deflation rate and the location of the plane approximating the upper east rift zone. These types of strong correlations lead to the wide range of acceptable values in the deflation rate and the volume point source depth. While the summit magma chamber has been deflating since the onset of the Pu'u O'o eruption, the rate of deflation here is 40% of that found by *Delaney et al.* [1993] for the 1983–1991 time period (0.002 km³/yr). However, Figure 10 shows that rates as high as 0.002 km³/yr fit the data reasonably well.

The deformation measurements around the station MPOO are of particular interest because many of Kilauea's larger earthquakes have nucleated in this region, including the recent M5.5 earthquake on June 30, 1997, the 1989, and the 1975 earthquakes (Figure 1). The velocities at stations in this region are inconsistent with the constant velocity model at the 95% confidence level. The nonsteady velocities and the deviation from the general pattern of extension along the south flank indicate that there may be unusual deformation in this region that can be detected geodetically. Permanent GPS stations, tiltmeters, or strainmeters are necessary to fully understand the deformation in this seismogenic region. Analysis of recent south flank seismicity through late 1993 shows a pattern of seismic quiescence in a region roughly bounded by PULA and 66YY [*Dieterich and Okubo*, 1996]. They found similar patterns of seismic quiescence prior to both the 1975 M7.2 and 1989 M6.1 earthquakes. So, while the highest rates of deformation and seismicity are occurring around the Hilina faults, major earthquake nucleation and unusual geodetic and seismic behavior are to be located farther east. It is not well understood why this region should behave anomalously. The September 1977 rift intrusion ended just north of Dieterich and Okubo's quiescent region. The last large rift intrusion, the January 1983 event that initiated the Pu'u O'o eruption, ended near the area where we have seen a possibly significant decrease in surface velocities on the south flank [*Owen et al.*, 1997]. The downrift extent of these intrusions may be causally related to these unusual seismic and geodetic results, or they may all share a common mechanical explanation.

The kinematic picture of Kilauea that we have generated supports the hypothesis that Kilauea's flank motion is gravitationally driven. If this were not the case, it would be difficult to explain the surface displacements along the western edge of the south flank where there have been no recent rift intrusions. It is clear from the data that the seaward velocities are significant west of the summit, the western edge of the actively

extending rift zone. Therefore it is likely that the western decollement is sliding because of gravitational forces. Although the landward basal fault dip of the optimal model may appear to preclude gravitational forces as the driving force, the gravitational potential energy can decrease if the basal fault dips landward, as long as the south flank's center of mass moves down. Whether the extension in the deep rift is contributing or reacting to the higher fault slip rates farther east is a question for further study.

5.   Conclusions

GPS campaigns on Kilauea between 1990 and 1996 measure high rates of horizontal displacement along the south flank. Coastal stations south of Makaopuhi Crater have average velocities of ~7 cm/yr, while stations north of the east rift zone and on the south flank's eastern and western ends are moving very slowly, if at all. This pattern of deformation is consistent with south flank motion observed since the 1975 $M7.5$ earthquake, although the 1990–1996 GPS velocities are substantially slower than those measured with trilateration in the years immediately following the earthquake. We measure high rates of extensional strain across the east rift zone. There is also shear strain between the central south flank and its distal ends. It is not presently known how or if the ends of the south flank catch up with the rapidly displacing central section.

Vertical velocities show subsidence of the rift system, with the maximum subsidence (~8 cm/yr) occurring south of the summit. There are two stations with significant uplift along the south flank coast. These rates are low (1–2 cm/yr) but argue against any significant normal faulting along the Hilina fault system between 1990 and 1996. The uplift along the coast also constrains the offshore extent of fault slip, since the vertical velocities are more sensitive than the horizontal velocities to variations in this parameter. Slip along the decollement produces subsidence over the islandward half of the fault plane and uplift over the seaward half.

The steep velocity gradient across the east rift zone requires that models include both deep rift dilation and fault slip along the decollement. Dilation deep within the rift zone is necessary to decouple the south flank motion from the north flank. This deep dilation occurs aseismically, as there is little microseismicity below 5 km within Kilauea's rift zones.

Using dislocation planes in a homogeneous elastic halfspace, the fault slip rates for the best fitting model are 23 and 28 cm/yr, with the higher rate on the eastern section of the fault plane. The GPS data and modeling provide estimates of the active fault geometry. The fault beneath the south flank is at least ~8 km deep. Likewise, rift dislocations at shallow depths (<4 km) in the middle east rift did not fit the data well. These results confirm other studies that place the seismogenic fault plane at the base of the volcanic pile and leveling and trilateration data that argue for deep dilation within the rift zone. The dip of the fault plane is not constrained well enough to say whether it is dipping islandward or seaward. However, faults dipping as much as ~20° seaward, as found by *Ando* [1979] for the 1975 $M7.2$ earthquake, can be ruled out. A lower bound can be placed on offshore extent of the actively slipping region. The model shows that dislocation planes that extended 12 km or more from the rift zone fit the data the best. The data appear to require that the same fault that slipped seismically in the 1975 earthquake is slipping aseismically at present (rates of ~20 cm/yr). Any viable mechanical model to explain this behavior must be consistent with the strong constraints placed on the deformation by the GPS data.

Appendix

A few stations within the network were reset, replaced, or destroyed over the time period discussed in this paper. The three sites without standard monuments (KALA, PKOA, and KULC) were all reset or replaced with nearby bench marks by 1996. Only one site, KMOA, has been destroyed by lava flows despite Pu'u O'o erupting continuously since 1983. The complete list of station resets is as follows: HP7 replaced HP6 in 1994; RKAL replaced KALO in 1995; GOTE replaced GOAT in 1993; KALR replaced KALA in 1995; and PULU replaced HULU after the bench mark was defaced in 1994. HULU was surveyed several times before 1994, but the data for HULU were not used in the velocity estimate since the derived displacements were erratic. KOAE replaced PKOA after 1993, but KOAE was sufficiently far from PKOA that it is considered a separate site in the velocity estimate.

Table 3 lists the campaigns included in the velocity estimate, the types of receivers used, and the number of stations observed. The first receivers, TI-4100 instruments, tracked only four satellites simultaneously but recorded dual-frequency code and full wavelength phase data. The Trimble SST, Ashtech LD-XII, and Ashtech MD-XII are L2-squaring receivers, which recorded single-frequency C/A code and dual-frequency phase data (half wavelength on L2). The Ashtech P-12, Trimble SSE, and Trimble SSI receivers recorded dual-frequency code and full wavelength phase data. The dramatic increase in the number of stations between 1992 and 1993 was due to an expansion and densification of the Kilauea network in 1993. Stations were added to cover the lower southwest rift and the east rift zone and to fill in the south flank. Between the Kilauea network campaigns in 1995 and 1996, HVO resurveyed the Chain of Craters Road network, a subset of stations near the summit and along the central south flank. This net-

Table 3.   Kilauea GPS Campaigns, 1990–1996

Campaign	Network	Receiver Type	Number of Sites
August–September 1990	Kilauea	TI-4100, Trimble SST	42
February–April 1992	Kilauea	Ashtech LD-XII, Ashtech MD-XII, Trimble SST	37
August 1993	Kilauea	Trimble SST, Trimble SSE, Ashtech P-12	62
July 1994	Kilauea	Trimble SSE	69
June 1995	Kilauea	Trimble SSE, Trimble SSI	57
September 1995	Chain of Craters	Trimble SSE, Trimble SSI	16
February 1996	Chain of Craters	Trimble SSE, Trimble SSI	15
April 1996	Chain of Craters	Trimble SSE, Trimble SSI	17
June 1996	Kilauea	Trimble SSE, Trimble SSI	63

work was surveyed every few months starting in late 1993 [*Miklius et al.*, 1997]. The minimum observing session for the surveys was 6 hours for the earlier surveys and 8 hours for the more recent measurements. Most of the surveys made repeat measurements at the majority of sites.

In all of the campaigns, one or two stations were measured semicontinuously. With numerous 24-hour-long occupations the station locations are better determined, so their velocities have smaller estimated errors. Two permanent GPS sites were installed in 1995. Uwekahuna Vault (UWEV) was installed early enough to be included in the 1995 campaign results, while the second site, Mauka Kipuka Nene (MANE), was installed in August 1995. The installation of permanent GPS sites in 1995 guaranteed that at least one station would be running throughout the campaign, freeing receivers and resources for surveying the rest of the network.

References

Ando, M., The Hawaii earthquake of November 29, 1975: Low dip angle faulting due to forceful injection of magma, *J. Geophys. Res.*, *84*, 7616–7626, 1979.

Arnadottir, T., and P. Segall, The 1989 Loma Prieta earthquake imaged from inversion of geodetic data, *J. Geophys. Res.*, *99*, 21,835–21,855, 1994.

Arnadottir, T., P. Segall, and P. Delaney, A fault model for the 1989 Kilauea south flank earthquake from leveling and seismic data, *Geophys. Res. Lett.*, *18*, 2217–2220, 1991.

Berg, B. A., Locating global minima in optimization problems by a random-cost approach, *Nature*, *361*, 708–710, 1993.

Beutler, G., I. Bauersima, W. Gurtner, M. Rothacher, and T. Schildknecht, GPS-techniques Applied to Geodesy and Surveying: Proceedings of the International GPS-workshop, Darmstadt, April 10–13, 1988, in *Lect. Notes Earth Sci.*, vol. 19, edited by E. Groten and R. Strauss, pp. 363–380, Springer-Verlag, New York, 1988.

Borgia, A., Dynamic basis of volcanic spreading, *J. Geophys. Res.*, *99*, 17,791–17,804, 1994.

Bryan, C. J., A possible triggering mechanism for large Hawaiian earthquakes derived from analysis of the 26 June, 1989, Kilauea south flank sequence, *Bull. Seismol. Soc. Am.*, *82*, 2368–2390, 1992.

Bürgmann, R., and P. Delaney, Deformation caused by the 1975 Kalapana earthquake beneath the south flank of Kilauea Volcano, Hawaii (abstract), *Eos Trans.. AGU*, *77*(46), Fall Meet. Suppl., F138, 1996.

Chen, W.-P., and J. Nabelek, Source parameters of the June 26, 1989, Hawaiian earthquake (abstract), *Eos Trans. AGU*, *71*, 562, 1990.

Clague, D. A., and R. P. Denlinger, Role of olivine cumulates in destabilizing the flanks of Hawaiian volcanoes, *Bull. Volcanol.*, *56*, 425–434, 1994.

Crosson, R. S., and E. T. Endo, Focal mechanisms and locations of earthquakes in the vicinity of the 1975 Kalapana earthquake aftershock zone 1970–1979: Implications for tectonics of the south flank of Kilauea Volcano, island of Hawaii, *Tectonics*, *1*, 495–542, 1982.

Davis, J. L., W. H. Prescott, J. L. Svarc, and K. J. Wendt, Assessment of Global Positioning System measurements for studies of crustal deformation, *J. Geophys. Res.*, *94*, 13,635–13,650, 1989.

Delaney, P. T., R. S. Fiske, A. Miklius, A. T. Okamura, and M. K. Sako, Deep magma body beneath the summit and rift zones of Kilauea Volcano, Hawaii, *Science*, *247*, 1311–1316, 1990.

Delaney, P. T., A. Miklius, T. Arnadottir, A. T. Okamura, and M. K. Sako, Motion of Kilauea Volcano during sustained eruption from

the Puu Oo and Kupaianaha vents, 1983–1991, *J. Geophys. Res.*, *98*, 17,801–17,820, 1993.

Delaney, P. T., R. P. Denlinger, M. Lisowski, A. Miklius, P. G. Okubo, A. T. Okamura, and M. K. Sako, Volcanic spreading at Kilauea, 1976–1996, *J. Geophys. Res.*, *103*, 18,003–18,024, 1998.

Dieterich, J. H., Growth and persistence of Hawaiian volcanic rift zones, *J. Geophys. Res.*, *93*, 4258–4270, 1988.

Dieterich, J. H., and P. Okubo, An unusual pattern of recurring seismic quiescence at Kalapana, Hawaii, *Geophys. Res. Lett.*, *23*, 447–450, 1996.

Du, Y., P. Segall, and H. Gao, Dislocations in inhomogeneous media via a moduli perturbation approach: General formulation and two-dimensional solutions, *J. Geophys. Res.*, *99*, 13,767–13,779, 1994.

Du, Y., P. Segall, and H. Gao, Quasi-static dislocations in three-dimensional inhomogeneous media, *Geophys. Res. Lett.*, *24*, 2347–2350, 1997.

Dvorak, J. J., F. W. Klein, and D. A. Swanson, Relaxation of the south flank after the 7.2-magnitude Kalapana earthquake, Kilauea Volcano, Hawaii, *Bull. Seismol. Soc. Am.*, *84*, 133–141, 1994.

Eissler, H. K., and H. Kanamori, A single-force model for the 1975 Kalapana, Hawaii earthquake, *J. Geophys. Res.*, *92*, 4827–4836, 1987.

Furumoto, A. S., and R. L. Kovach, The Kalapana earthquake of November 29, 1975: An intraplate earthquake and its relation to geothermal processes, *Phys. Earth Planet. Inter.*, 197–208, 1979.

Gillard, D., A. M. Rubin, and P. Okubo, Highly concentrated seismicity caused by deformation of Kilauea's deep magma system, *Nature*, *384*, 343–346, 1996.

Got, J.-L., J. Frechet, and F. W. Klein, Deep fault plane geometry inferred from multiplet relative relocation beneath the south flank of Kilauea, *J. Geophys. Res.*, *99*, 15,375–15,386, 1994.

Gregorius, T., *GIPSY-OASIS II: A User's Guide*, Univ. Newcastle, Newcastle, England, 1996.

Klein, F. W., R. Y. Koyanagi, J. S. Nakata, and W. R. Tanigawa, The seismicity of Kilauea's magma system, in *Volcanism in Hawaii*, edited by R. W. Decker, T. L. Wright, and P. H. Stouffer, *U.S. Geol. Surv. Prof. Pap.*, *1350*, 1019, 1987.

Larson, K., F. H. Webb, and D. C. Agnew, Application of Global Positioning System to crustal deformation measurement, 2, The influence of errors in orbit determination networks, *J. Geophys. Res.*, *96*, 16,547–16,565, 1991.

Lipman, P. W., J. P. Lockwood, R. T. Okamura, D. A. Swanson, and K. M. Yamashita, Ground deformation associated with the 1975 magnitude-7.2 earthquake and resulting changes in activity of Kilauea Volcano, Hawaii, *U.S. Geol. Surv. Prof. Pap.*, *1276*, 45 pp., 1985.

Lisowski, M., S. Owen, and P. Segall, The Kilauea Volcano, Hawaii, continuous GPS networks: Recent results (abstract), *Eos Trans. AGU*, *77*(46), 808, Fall Meet. Suppl., 1996.

Ma, K.-F., H. Kanamori, and K. Satake, Mechanism of the 1975 Kalapana, Hawaii, earthquake inferred from tsunami data, *J. Geophys. Res.*, *104*, 13,153–13,168, 1999.

Miklius, A., F. Colima, R. Denlinger, M. Lisowski, S. Owen, M. Sako, and P. Segall, Global Positioning System measurements on the island of Hawaii: 1993 through 1996, *U.S. Geol. Surv. Open File Rep.*, *97–698, 1997.*

Mogi, K., Relations between the eruptions of various volcanoes and the deformations of the ground surfaces around them, *Bull. Earthquake Res. Inst. Univ. Tokyo*, *36*, 111–123, 1958.

Moore, J. G., and R. K. Mark, Morphology of the island of Hawaii, *GSA Today*, *2*, 257–259, 1992.

Murray, M., G. Marshall, M. Lisowski, and R. Stein, The 1992 $M = 7$ Cape Mendicino, California, earthquake: Coseismic deformation a the south end of the Cascadia megathrust, *J. Geophys. Res.*, *101*, 17,707–17,725, 1996.

Okada, Y., Surface deformation due to shear and tensile faults in a half-space, *Bull. Seismol. Soc. Am.*, *75*, 1135–1154, 1985.

Owen, S., P. Segall, J. Freymueller, A. Miklius, R. Denlinger, T. Arnadottir, M. Sako, and R. Bürgmann, Rapid deformation of the south flank of Kilauea Volcano, Hawaii, *Science*, *267*, 1328–1332, 1995.

Owen, S., A. Miklius, P. Segall, M. Lisowski, and M. Sako, Displacements from the June 30, 1997, $M5.5$ Kilauea south flank earthquake and preceding decrease in slip rate (abstract), *Eos Trans. AGU*, *78*(46), Fall Meet. Suppl., F166, 1997.

Owen, S., P. Segall, M. Lisowski, and A. Miklius, Distribution of fault

slip and rift dilation on Kilauea Volcano, Hawaii (abstract), *Eos Trans. AGU*, *79*(45), F36, Fall Meet. Suppl., 1998.

Rothacher, M., G. Beutler, W. Gurtner, T. Schildknect, and U. Wild, Documentation for Bernese GPS Software version 3.2, Univ. Bern, Bern, Switzerland, 1990.

Rowan, L. R., and R. Clayton, The three-dimensional structure of Kilauea Volcano, Hawaii, from travel time tomography, *J. Geophys. Res.*, *98*, 4355–4375, 1993.

Rubin, A. M., D. Gillard, and J.-L. Got, A reinterpretation of seismicity associated with the January 1983 dike intrusion at Kilauea Volcano, Hawaii, *J. Geophys. Res.*, *103*, 10,003–10,015, 1998.

Ryan, M. P., The mechanics and three-dimensional internal structure of active magmatic systems; Kilauea Volcano, Hawaii, *J. Geophys. Res.*, *93*, 4213–4248, 1988.

Stearns, H. T., and W. O. Clark, Geology and water resources of the Kau District, Hawaii (including parts of Kilauea and Mauna Loa volcanoes), *U.S. Geol. Surv.*, *Water Supply Pap.*, *616*, 194 pp., 1930.

Swanson, D. A., W. A. Duffield, and R. S. Fiske, Displacement of the south flank of Kilauea Volcano: The result of forceful intrusion of magma into the rift zones, *U.S. Geol. Surv. Prof. Pap.*, *963*, 39 pp., 1976.

Thurber, C. H., Seismic detection of the summit magma complex of Kilauea Volcano, Hawaii, *Science*, *223*, 165–167, 1984.

Thurber, C. H., and A. E. Gripp, Flexure and seismicity beneath the south flank of Kilauea Volcano and tectonic implications, *J. Geophys. Res.*, *93*, 4271–4278, 1988.

Tilling, R. I., R. Y. Koyanagi, P. W. Lipman, J. P. Lockwood, J. G. Moore, and D. A. Swanson, Earthquake and related catastrophic events, island of Hawaii, November 29, 1975, a preliminary report, *U.S. Geol. Surv. Circ.*, *C 740*, 32 pp., 1976.

Wallace, M., and P. Delaney, Deformation of Kilauea Volcano during 1982 and 1983: A transition period, *J. Geophys. Res.*, *100*, 8201–8219, 1995.

Wyss, M., A proposed source model for the great Kau, Hawaii, earthquake of 1868, *Bull. Seismol. Soc. Am.*, *78*, 1450–1462, 1988.

Yang, X., P. M. Davis, P. T. Delaney, and A. T. Okamura, Geodetic analysis of dike intrusion and motion of the magma reservoir beneath the summit of Kilauea Volcano, Hawaii: 1970–1985, *J. Geophys. Res.*, *97*, 3305–3324, 1992.

Zucca, J. J., and D. Hill, Crustal structure of the southeast flank of Kilauea Volcano, Hawaii, from seismic refraction measurements, *Bull. Seismol. Soc. Am.*, *70*, 1149–1159, 1980.

Zumberge, J. F., M. B. Heflin, D. C. Jefferson, M. M. Watkins, and F. H. Webb, Precise point positioning for the efficient and robust analysis of GPS data from large networks, *J. Geophys. Res.*, *102*, 5005–5017, 1997.

R. Denlinger, U.S. Geological Survey, Cascades Volcano Observatory, 5400 MacArthur Blvd., Vancouver, WA. (roger@mailvan.wr.usgs.gov)

M. Lisowski, A. Miklius, and M. Sako, U.S. Geological Survey, Hawaii Volcano Observatory, POB51, Hawaii National Park, HI 96718. (mlisowski@usgs.gov; asta@usgs.gov; sako@usgs.gov)

S. Owen, Department of Earth Sciences, University of Southern California, 3651 Trousdale Parkway, Los Angeles, CA 90089-0740. (owen@terra.usc.edu)

P. Segall, Department of Geophysics, Stanford University, Stanford CA 94305. (segall@stanford.edu)